Langmuir, Volume 41, Issue 46, November 2025, pp. 31639-31648
DOI:10.1021/acs.langmuir.5c04844

# Dual-Gradient Wettability-Patterned Surface for Droplet Rectification and Targeted Transport

Fujian Zhang[1], Baochen Cui[1], Zhen Liu[2], Kehan Huang[1], Yunyun Song[1], Patrick Verdin[3], Zhongqiang Zhang[1, †]

[1] *School of Mechanical Engineering, Jiangsu University, Zhenjiang 212013, PR China*

[2] *School of Naval Architecture and Ocean Engineering, Jiangsu University of Science and Technology, Zhenjiang 212003, PR China*

[3] *Faculty of Engineering and Applied Science, Cranfield University, Cranfield, MK43 0AL, UK*

[†] Corresponding Author. zhangzq@ujs.edu.cn (Zhongqiang Zhang)

## Abstract

Droplet self-transport holds significant implications for applications such as water harvesting, microreactors, and microfluidic chips. Achieving precise and efficient droplet self-transport is therefore crucial. Herein, a dual-gradient wettability-patterned surface (DWPS) incorporating both wettability and structural gradients is proposed, where the wettability gradient facilitates ultrafast droplet transport while the structural gradient serves to rectify the transport direction, collectively achieving directional droplet rectification and ultrafast targeted self-transport. The influence mechanism of energy conversion on droplet self-transport behavior during oscillatory motion is elucidated. The oscillatory behavior during droplet self-transport can be effectively suppressed through the droplet coalescence strategy. Compared to the single wettability or structural gradient surfaces, the structural gradient surface exhibits the lowest transport efficiency. Although the droplet self-transport efficiency on the DWPS is also lower than that on the wettability gradient surface, it enables precise droplet transport. The mechanisms underlying the self-transport behavior and efficiency variations on the three model surfaces are revealed through the analysis of the relationship between solid-liquid interfacial energy and droplet potential energy. These findings provide a theoretical foundation for the design of functional surfaces aimed at achieving precise droplet self-transport.



Published by ACS. This is the Author Accepted Manuscript issued with: Creative Commons Attribution License (CC:BY 4.0).
The final published version (version of record) is available online at DOI:10.1021/acs.langmuir.5c04844. Please refer to any applicable publisher terms of use.

**Keywords:** wettability-patterned surface, wettability gradient, structural gradient, droplet self-transport, targeted transport.

## Introduction

Droplet transport is not only ubiquitous in nature but also holds significant value in fields such as water collection, microreactors, microfluidic chips, oil-water separation and biomedical detection.[1-6] Understanding droplet transport behavior and its underlying mechanisms provides a critical theoretical foundation for the design of functional devices. Nature offers abundant examples of droplet propulsion: for instance, the multi-scale structure on the surface of pitcher plants enhances capillary lifting forces in the direction of droplet transport while pinning the contact line in the opposite direction to achieve unidirectional liquid transport[7, 8]; the hairy surface of sarracenia features unique multi-level microchannel structures, enabling rapid formation of wetting water films that facilitate fast droplet transport[9]. Inspired by these fascinating biological structures, functional surfaces such as concave curved pyramid-shaped fibers and superhydrophobic ordered scaly structures have been proposed to achieve droplet self-transport[10, 11]. Notably, by mimicking the Araucaria leaf, a capillary ratchet was designed to generate an asymmetric 3D diffusion profile, enabling reverse transport of liquids with different surface tensions[12]. A study reported in Nature Materials demonstrated the printing of gradient density surface charges on substrates via droplet impact, driving droplets at high speeds over long distances without requiring additional energy input, thus realizing programmable surfaces for droplet transport[13]. Based on the presence or absence of external energy input, droplet propulsion can be categorized into external field-driven and self-driven droplet transport. External field-driven transport relies on electric fields, temperature gradients, light fields, magnetic fields, or mechanical vibrations to provide external energy for droplet motion.[14-19] For example, the directional transport and programmable arrangement of room-temperature liquid metals under an electric field[20], and the directional bouncing transport of droplet impact on surfaces with asymmetric structures[21, 22]. In contrast, self-driven droplet transport achieves motion by breaking droplet symmetry through surface wettability

gradients, morphological gradients, or stiffness gradients, without external energy input.[23-30] Compared to external field-driven methods, droplet self-transport eliminates the need for external energy sources and field control, simplifying system design, enabling miniaturization and portability, and making it more suitable for constructing large-scale, complex droplet transport networks, particularly in biological and medical applications.[3, 31]

The controllability of droplet self-transport is a key performance metric. Novel topological liquid diode structures restrict liquid motion in three directions on a surface via pinning effects, enabling unidirectional long-distance self-transport of continuous liquids[32]. Biomimetic wedge-shaped grooves with gradual wettability variations reduce energy barriers at groove junctions, facilitating continuous acceleration and directional long-distance droplet self-transport[33]. However, many applications require converging all droplets on a surface to a single point to enhance device performance. For example, in high-sensitivity biochemical detection, numerous dispersed droplets containing target molecules must be driven to merge at a single point to concentrate and enrich the target molecules, ultimately achieving detectable concentrations in the coalesced droplet.[3, 34] In efficient mixing and chemical reactions, droplets containing different reactants need to be transported from various paths to a common mixing point (reaction site) for merging to rapidly initiate chemical reactions.[3, 34] Although structured surfaces such as topological fluid diodes[32], wedge-shaped surfaces[35, 36], and gradient grooves[33, 37] enable directional droplet transport, they impose requirements on droplet starting positions, making it challenging to achieve full-plane droplet manipulation and convergence. Wettability gradient surfaces can achieve directional self-transport of droplets across the entire surface through wettability patterning[38]. However, such surfaces are susceptible to environmental disturbances, causing droplets to deviate from their intended paths.[39] Additionally, the endpoint of droplet transport on wettability gradient surfaces is often tied to the starting position, making it difficult to achieve targeted self-transport of all droplets to a single point.[39] Although recent studies have demonstrated that droplets on axisymmetric curved surfaces can exhibit uphill motion and move toward the apex, their transport velocity

remains slow, and the application of surface gradients over large areas poses significant challenges[40]. Therefore, achieving efficient and targeted self-transport of droplets on functional surfaces remains challenging.

In this work, a dual-gradient wettability-patterned surface (DWPS) combining wettability and structural gradients is proposed to enable ultrafast and targeted droplet self-transport. The self-transport behavior of droplets on this surface is investigated using molecular dynamics simulations. The effects of wettability and structural gradients on droplet transport velocity and direction are analyzed, and the influence of energy conversion on droplet self-transport behavior is explored. A theoretical relationship between friction force and droplet velocity, contact area, and solid-liquid interfacial interaction strength during self-transport is established. The suppressive effect of droplet coalescence on oscillatory behavior during self-transport is examined. A comparative study of targeted self-transport behavior on single wettability gradient surface, single structural gradient surface, and DWPS is conducted, highlighting the efficient targeted self-transport capability and long-distance driving capability for small droplets of the dual-gradient surface. The findings provide a theoretical basis for the design of functional surfaces aimed at achieving rapid and precise droplet self-transport.

## Model and Methods

The droplet self-transport model consists of a water nanodroplet (8 nm diameter, TIP4P-Ew model[41]) and a wettability-patterned graphene sheet (53 nm × 30 nm), as shown in Figure 1. The simulation box measures 58 nm × 35 nm × 12 nm (length × width × height). The graphene exhibits progressively enhanced wettability along the *w*-direction, with each wettability zone having a *y*-width of 2 nm and an inter-zone angle $\alpha = 10°$. This spatially modulated wettability patterning establishes dual wettability-structural gradients that synergistically drive droplet transport. Point *O* on the axis serves as the coordinate origin. The droplet's initial position is at (0, 11) nm in the Figure 1(a), with its bottom surface maintaining an equilibrium distance of 3.28 Å above the DWPS (corresponding to the C-O atomic separation distance).

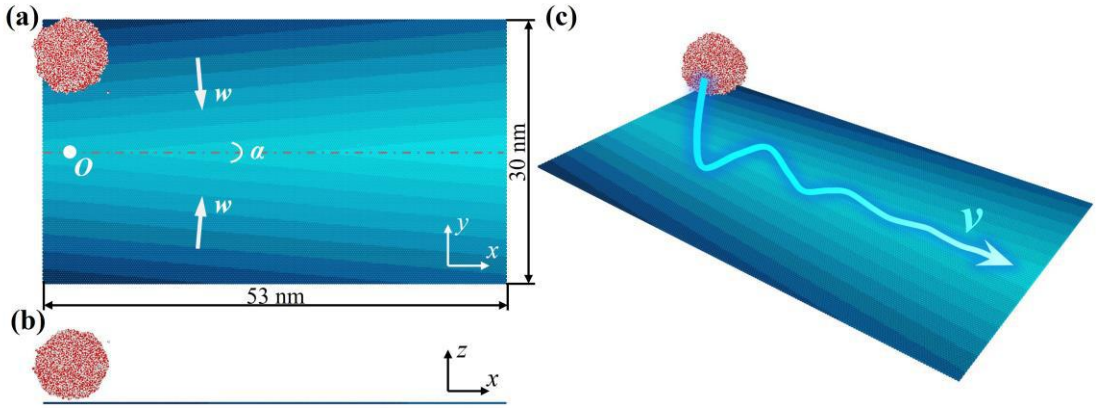



Figure 1 The model of dual-gradient wettability-patterned surface (DWPS) for droplet transport. (a-b) The graphene sheet with linear wettability gradient along the *w* direction, the included angle $\alpha$ between same-wettability zones is 10°, the graphene sheet measures 53 nm in length and 30 nm in width, the diameter of the water droplet is 8 nm. (c) Schematic illustration of droplet transport pathways on the DWPS.

Molecular dynamics simulations are performed using the open-source LAMMPS package under the NVT ensemble with a timestep of 1 fs (the minimum timestep). Interatomic interactions are modeled by Lennard-Jones potentials, where C-O interactions are calculated using the Lorentz-Berthelot mixing rules. The interatomic interaction parameters were set as follows: the potential well depths $\varepsilon_{OO} = 7.06$ meV, $\varepsilon_{CC} = 3.73$ meV, $\varepsilon_{CO} = 5.13$ meV; the equilibrium distance $\sigma_{OO} = 3.16$ Å, $\sigma_{CC} = 3.40$ Å, $\sigma_{OO} = 3.28$ Å.[41, 42] The potential well depth $\varepsilon$ reflects the strength of interatomic interactions, allowing for wettability patterning by modulating the $\varepsilon$ value between carbon and oxygen (C-O) atoms. To quantify this, we introduce an interaction intensity coefficient $k$ to characterize the relative difference in interaction strength between distinct wettability zones and the reference value. This coefficient $k$ directly determines the C-O potential well depth $\varepsilon_{C_iO}$ in each wettability zone, where $\varepsilon_{C_iO} = k\varepsilon_{CO}$, with $\varepsilon_{CO} = 5.13$ meV being the reference interaction strength. The specific parameter values for each wettability zone are summarized in Table 1. The Lennard-Jones potential parameters between hydrogen (H) atoms and all other atomic species were uniformly set to zero ($\varepsilon = 0, \sigma = 0$), effectively disabling van der Waals interactions for hydrogen in the system.

Table 1 The parameters of the interaction strength between water molecules and graphene atoms for different wettability zones of the DWPS. The distribution of wettability zones can be found in Figure S1. The $k$ is the ratio of the interaction strength between different wettability zones to the reference value (Zone 3).

| Zone | 1 | 2 | 3 | 4 | 5 | 6 | 7 | 8 | 9 | 10 |
|---|---|---|---|---|---|---|---|---|---|---|
| $k$ | 1.25 | 1.125 | 1 | 0.875 | 0.75 | 0.625 | 0.5 | 0.375 | 0.25 | 0.125 |
| $\varepsilon_{CO}$ (meV) | 641 | 577 | 513 | 449 | 385 | 321 | 257 | 192 | 128 | 64 |

## Results and Discussion

### Droplet Rectification and Targeted Transport on DWPS

To investigate the targeted self-transport characteristics of droplets on the DWPS, we systematically studied the influence of initial positions on droplet motion. Four distinct initial positions were examined: Droplet 1 (0, 0), Droplet 2 (0, 11), Droplet 3 (20, 11), and Droplet 4 (35, 11) nm (coordinates relative to the surface origin). As demonstrated in Figure 2(a), all droplets from different initial positions ultimately converged to the same predetermined target point, achieving precise position-controlled self-transport (Movie S1). This remarkable convergence behavior confirms the surface's ability to guide droplets to designated locations regardless of their initial positions.

Compared to Droplet 1, the centroids of the other three droplets were initially off the central axis of the DWPS, resulting in a combined motion of $y$-direction oscillation and $x$-direction propulsion. To quantify the self-transport behavior, the displacement and velocity of the droplets along both $x$- and $y$-directions were analyzed over time. To eliminate boundary effects on droplet transport, data collection in $x$-direction transport was terminated when the droplet's advancing contact line reached 1.5 nm from the right boundary of DWPS (Figure S2). All four droplets exhibited rightward motion, with Droplet 2 achieving greater displacement than droplet 1 at the same time point by the end of transport, indicating higher transport efficiency despite its longer trajectory (Figure 2b). In terms of velocity, Droplet 1—initially positioned on the $x$-axis—showed

no *y*-direction oscillation and accelerated faster, reaching a peak speed of 42.7 m/s (Figure 2c and Figure S3). The other three droplets, initially offset from the *x*-axis, exhibited slower acceleration as they first moved toward the central axis of the DWPS under wettability gradient-driven forces. However, Droplet 2 attained a higher maximum *x*-direction velocity of 46.5 m/s and sustained prolonged high-speed motion, likely due to its *y*-direction oscillation. The *y*-direction motion analysis revealed that the droplets rapidly approached the *x*-axis, with their oscillation amplitudes gradually decaying over time, indicating that the DWPS effectively suppressed longitudinal (*y*-direction) oscillations (Figure 2d). Notably, the droplets achieved a maximum *y*-direction velocity of 132.8 m/s with rapid reversal, highlighting the surface's exceptional rectification capability (Figure 2e).

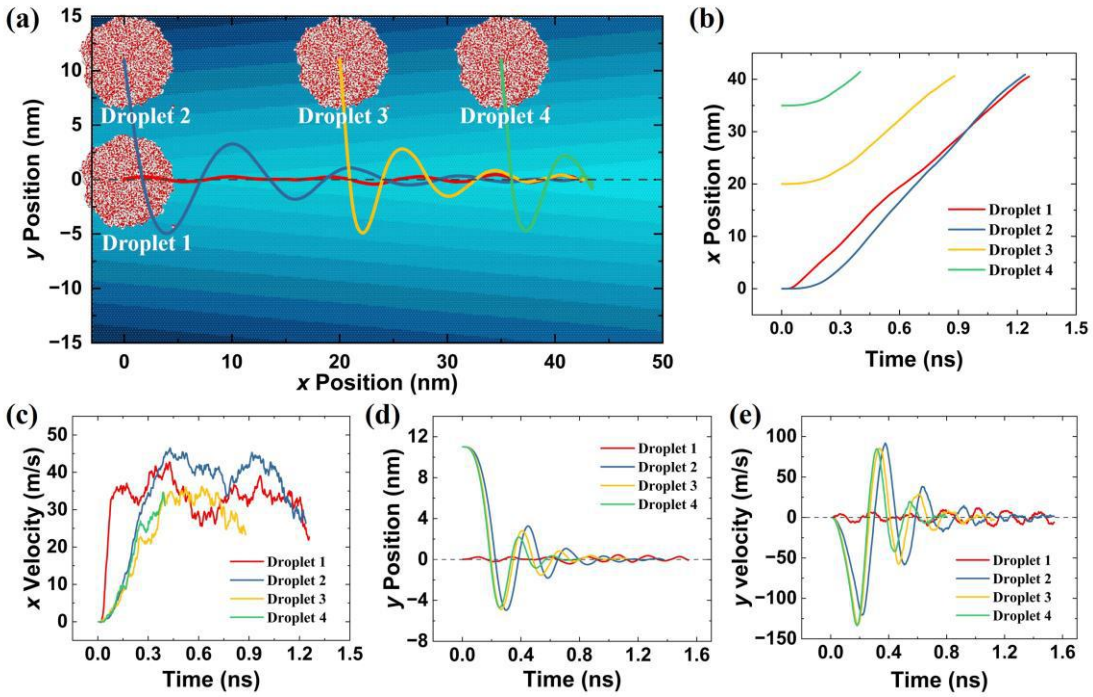



Figure 2 The self-transport behavior of droplet on the DWPS. (a) The transport trajectories of droplets from different initial positions. The initial coordinates (*x*, *y*) of droplets 1, 2, 3, and 4 are (0, 0), (0, 11), (20, 11), and (35, 11) nm, respectively. (b) The displacements and (c) velocities of the four droplets in the *x*-direction. (d) The displacements and (e) velocities of the four droplets in the *y*-direction.

**Mechanism of Droplet Rectification and Targeted Transport**

The self-transport behavior of droplets was analyzed from force and energy

perspectives, with particular focus on oscillating Droplet 2. The *x*-direction force on the Droplet 2 initially increased progressively, enabling rapid axial acceleration, then diminished to fluctuate near zero, sustaining stable high-speed motion (Figure 3a). The *y*-direction force exhibited periodic sign reversal, consistently directing the droplet toward the central axis of the DWPS. Notably, the *x*-direction driving force was one order of magnitude smaller than its *y*-direction counterpart, explaining why off-axis droplets rapidly converged toward the central axis. Energetically, the droplet-DWPS interfacial interaction energy and droplet potential energy constituted the driving sources. For Droplet 1 (on-axis), nearly constant potential energy meant the self-transport was powered primarily by decreasing interfacial interaction energy (Figure S4). However, the rate of this energy reduction became slower than that of Droplet 2 after ~0.3 ns, resulting in a weaker driving force and a lower velocity for Droplet 1 beyond this time point. Droplet 2's *y*-oscillation involved dynamic energy conversion: Initially, sharp decreases in both potential and interaction energies provided strong propulsion (Figure 3b). At peak *y*-velocity, rapid deceleration converted kinetic energy back into rising droplet potential and interfacial interaction energies, demonstrating kinetic energy recovery. Subsequent oscillations showed gradually damped energy exchange amplitudes as *y*-oscillation attenuated. Globally, while potential energy remained stable, the sharply declining interfacial interaction energy delivered robust, directional propulsion for targeted self-transport.

To characterize the interfacial energy landscape, we developed a probing model on the DWPS by arranging 15 water molecules along the +*y* boundary with 3 nm inter-molecular spacing, which were then driven toward the -*y* direction at 2 m/s (Figure 3c). The interfacial energy distribution exhibits a gradual decrease toward the right-central zone of the DWPS, creating a distinct energy valley, as shown in Figure 3d. Governed by the principle of energy minimization, droplets invariably migrate toward lower energy states, ensuring their spontaneous transport to the energy valley's minimum point regardless of initial positions, thereby achieving precise targeted transport.

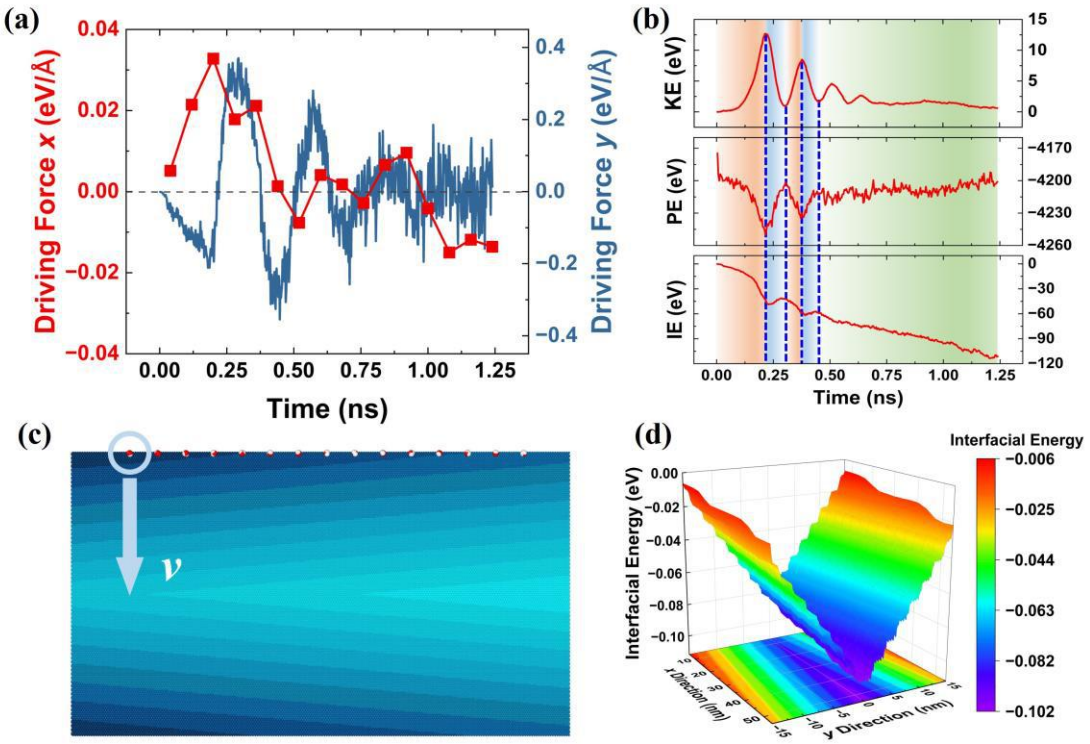



Figure 3 Forces and energy variations during droplet self-transport on the DWPS. (a) Forces acting on self-transport Droplet 2 in *x*- and *y*-directions. (b) Temporal evolution of droplet kinetic energy (KE), potential energy (PE), and droplet-DWPS interfacial interaction energy (IE). (c) The model for DWPS interfacial energy characterization. At the boundary in the +*y* direction, 15 water molecules spaced 3 nm apart move uniformly at 2 m/s along the -*y* direction. (d) The interfacial energy distribution of DWPS.

**Theoretical Analysis of Droplet Rectification and Targeted Transport**

Theoretically, the droplet's motion is governed by the driving force $F_d$ generated by the wettability gradient and the interfacial frictional resistance $F_f$: $F = F_d - F_f$. Due to the patterned arrangement of wettability zones, the driving force $F_d$ arising from the wettability gradient can be divided into three distinct stages: Stage I, where the droplet does not contact the central axis of the DWPS; Stage II, where the droplet contacts the central axis of the DWPS; and Stage III, where the droplet's central line in the *x*-direction coincides with the central axis of the DWPS (Figure 4). The driving force $F_d$ on the wettability gradient surface can be expressed as: $F_d = \gamma A \delta S$, where $\gamma$ is the surface tension of the droplet, $A$ is the contact area between the droplet and the

surface, and $\delta S$ represents the wettability difference.[38, 43] For Stage I, $F_d$ can be written as:

$$F_d = \gamma A \frac{\cos\theta_{B_2} - \cos\theta_{B_1}}{l_{12}}, \tag{1}$$

where $B_1$ and $B_2$ are the tangent points between the droplet's contact line contour and the isowettability lines, $\theta_{B_1}$ and $\theta_{B_2}$ are the contact angles at the two points, and $l_{12}$ is the distance between the two points, representing the length of the contact line along the wettability gradient direction. In Stage II, $F_d$ can be expressed as:

$$F_d = \gamma A_1 \frac{\cos\theta_Q - \cos\theta_{B_1}}{l_1} + \gamma A_2 \frac{\cos\theta_Q - \cos\theta_{B_2}}{l_2}, \tag{2}$$

where $A_1$ and $A_2$ represent the contact areas between the droplet and the upper/lower regions of the DWPS central axis, respectively. Point $Q$ is the contact point between the droplet's advancing contact line and the DWPS central axis, $\theta_Q$ is the contact angle at this point, $l_1$ is the contact line length along the wettability gradient direction in region $A_1$, and $l_2$ is the corresponding length in region $A_2$. For Stage III, the droplet's oscillation in the $y$-direction is largely suppressed, and the droplet moves along the $+x$ direction. Here, $F_d$ can be represented as:

$$F_d = \gamma A \frac{\cos\theta_Q - \cos\theta_{B_1}}{l_1}. \tag{3}$$

By comparing these three equations, we observe that Equations 1 and 3 are special cases of Equation 2. Specifically, when $A_2$ in Equation 2 is zero, $l_{12}$ represents the contact line along the wettability gradient direction, reducing Equation 2 to Equation 1. When $A_1$ and $A_2$ in Equation 2 are equal, $l_1$ and $l_2$, as well as $\cos\theta_{B_1}$ and $\cos\theta_{B_2}$, become identical, yielding Equation 3. Thus, the driving forces $F_d$ in all three phases can be unified under Equation 2, leading to the general expression for the droplet's driving force in the $x$-direction:

$$F_{dx} = \left( \gamma A_1 \frac{\cos\theta_Q - \cos\theta_{B_1}}{l_1} + \gamma A_2 \frac{\cos\theta_Q - \cos\theta_{B_2}}{l_2} \right) \sin\frac{\alpha}{2}. \tag{4}$$

The relationship between solid-liquid interfacial interaction strength and contact

angle is shown in Figure 5a, where the droplet contact angle exhibits an approximately linear correlation with the interfacial interaction strength. Thus, the relationship between contact angle $\theta$ and interfacial interaction strength $k$ can be expressed as:

$$\theta = ak + C, \tag{5}$$

where $a$ is the slope, representing the rate of change of the contact angle with interaction strength, and $C$ is a constant. Since the distribution of interfacial interaction strength $k$ is position-dependent along the wettability gradient direction $w$, the above equation can be rewritten as:

$$\theta(w) = ak(w) + C, \tag{6}$$

Assuming that the wettability transition along the $w$-direction is smooth (i.e., $k(w)$ is differentiable), the corresponding differential equation can be derived as:

$$\frac{dk}{dw} = f(w), \tag{7}$$

$$k(w) = \int f(w)dw + D, \tag{8}$$

where $D$ is an another constant. This allows the determination of the contact angle $\theta(w)$ at different positions along the wettability gradient direction $w$:

$$\theta(w) = a\left(\int f(w)dw + D\right) + C. \tag{9}$$

In our model of DWPS, the interaction strength $k$ follows a linear and uniform distribution along the $w$-direction, meaning the rate of change in interaction strength $f(w) = dk/dw$ is a constant denoted as $m$. Therefore, the Equation 9 simplifies to:

$$\theta(w) = a\left(\int mdw + D\right) + C. \tag{10}$$

Consequently, the contact angles at points $B_1$ and $B_2$ can be expressed as:

$$\theta_{B_1} = aml_1 + \theta_Q, \tag{11}$$

$$\theta_{B_2} = aml_2 + \theta_Q. \tag{12}$$

Based on these, the general expression for the droplet's driving force $F_{dx}$ in the $x$-direction (Equation 4) can be further represented as:

$$F_{dx}=\left(\gamma A_1\frac{\cos\theta_Q-\cos\left(aml_1+\theta_Q\right)}{l_1}+\gamma A_2\frac{\cos\theta_Q-\cos\left(aml_2+\theta_Q\right)}{l_2}\right)\sin\frac{\alpha}{2}. \quad (13)$$

To more intuitively assess the driving force in the *y*-direction $F_{dy}$, we calculate it based on the contact angles and contact line lengths at the upper and lower points (points C and D) of the droplet's contact line contour:

$$F_{dy}=\gamma\left(A_1+A_2\right)\frac{\cos\theta_C-\cos\theta_D}{l_3}. \quad (14)$$

When the contact angle $\theta_C$ at point *C* is greater than $\theta_D$ at point *D*, it indicates that the droplet's centroid lies above the DWPS central axis, resulting in a negative $F_{dy}$ that drives the droplet toward the DWPS central axis. Conversely, when $\theta_C$ is less than $\theta_D$, the centroid is below the axis, producing a positive $F_{dy}$ that similarly drives the droplet toward the DWPS central axis.

The analysis demonstrates how the wettability gradient and contact line dynamics govern the droplet's directional motion, with the unified Equation 13 capturing the driving force across all stages of movement. The *y*-direction force Equation 14 further ensures the droplet's convergence to the DWPS central axis, regardless of its initial position.

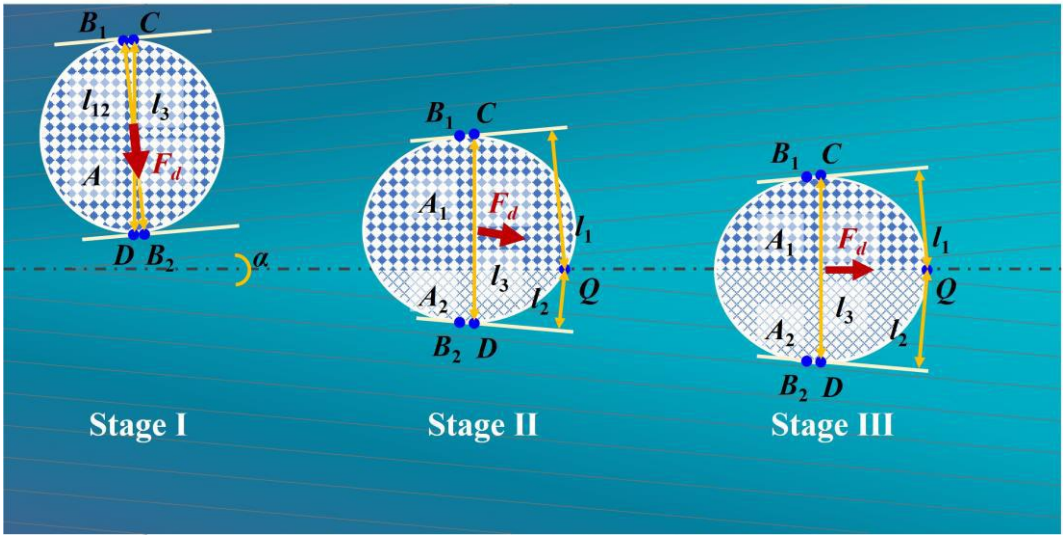



Figure 4. Analysis of droplet transport mechanism on the DWPS. Droplet transport is divided into three stages: Stage I—the droplet does not contact the DWPS central axis; Stage II—the droplet contacts the DWPS central axis; Stage III—the droplet's central axis aligns with the DWPS central axis. The driving force $F_d$ of the droplet continuously

changes in both magnitude and direction as its position varies.

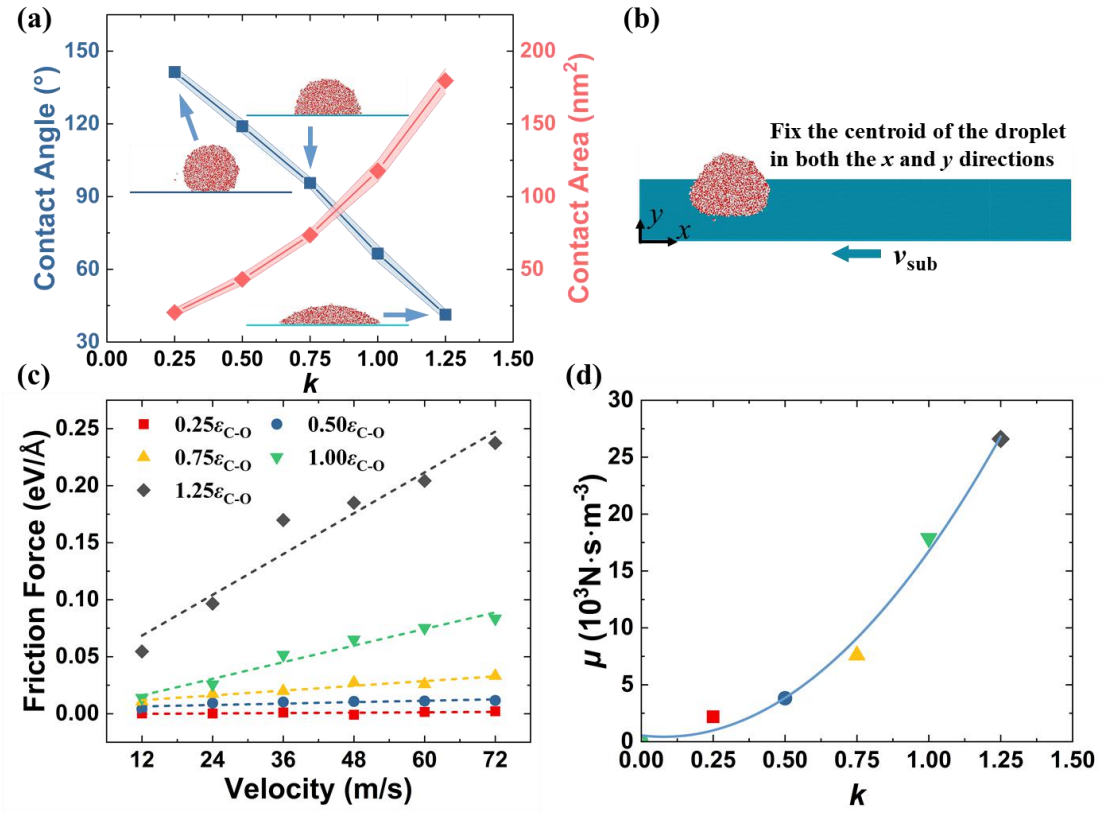



Figure 5 Analysis of friction force of droplet self-transport. (a) Influence of interaction strength $k$ between droplet and graphene on contact angle and contact area. (b) Model of an 8 nm diameter droplet on graphene sheet (26 nm × 50 nm) for interfacial friction analysis. (c) Friction force versus transport velocity at the interaction strength $k$ from 0.25 to 1.25. (d) Relationship between friction coefficient and interfacial interaction strength $k$.

On the other hand, interfacial friction force $F_f$ is another critical factor influencing droplet self-transport behavior. To investigate this, we established a motion model for droplet on graphene surfaces with varying wettability (Figure 5b), restricting the motion of the droplet's center of mass in both the $x$ and $y$ directions while driving the graphene sheet at a constant velocity ranging from 12 m/s to 72 m/s along the -$x$ direction. Figure 5c shows the relationship between friction force $F_f$ and relative motion velocity for droplets on graphene sheet under different solid-liquid interaction strengths $k$. The friction force $F_f$ consistently increases with velocity $v$ across all

interaction strengths. Linear regression reveals a proportional relationship between interfacial friction force and velocity ( $F_f \propto v$ ). Furthermore, as the solid-liquid interaction strength $k$ increases, the contact angle gradually decreases while the contact area $A$ expands (Figure 5a). We further analyzed the friction coefficient $\mu$ ( $\mu = F_f / vA$ ) as a function of interaction strength $k$ (Figure 5d), demonstrating that $\mu$ increases with $k$. A fitted curve yields the relationship $\mu = 19.2(k - 0.078)^2 + 0.43$, indicating that $\mu$ is approximately proportional to $k^2$ ( $\mu \propto k^2$ ). Consequently, the interfacial friction force $F_f$ can be expressed as:

$$F_f = nk^2 vA , \tag{15}$$

where $n$ is a friction correction coefficient accounting for system-specific adjustments.

**Oscillation Suppression via Droplet Coalescence**

Although DWPS can achieve targeted droplet transport, suppressing droplet oscillation is crucial for enhancing system stability in certain applications. To address this, we developed a droplet collision-coalescence and self-transport model (Figure 6a). Two droplets of equal volume (with a combined volume equivalent to an 8 nm-diameter droplet) were initially positioned at (0, 11) nm and (0, -11) nm, respectively. The droplets first rapidly moved toward the DWPS central axis, collided and coalesced, and subsequently underwent directional self-transport to the right (Movie S2). The coalescence dynamics were analyzed using the mean squared displacement (MSD), revealing that droplet fusion initiated at ~0.15 ns and completed by ~0.58 ns (Figure 6b). Post-coalescence, the coalesced droplet exhibited significantly greater acceleration than Droplet 2, attributed to collision-induced enhanced spreading along the $+x$ direction (Figure 6c). However, after reaching maximum velocity, the coalesced droplet experienced rapid deceleration. This occurs because collision and coalescence dissipate kinetic energy by abruptly nullifying the $y$-direction velocity, preventing energy recovery through solid-liquid interfacial energy or potential energy conversion, unlike the case with Droplet 2 (Figure S5). Consequently, the transport efficiency of the coalesced droplet was slightly lower than that of individual Droplets 1 and 2 (Figure 6d). The motion trajectories of the upper and lower droplets were plotted, and the

average of their *y*-direction coordinates was used to represent the trajectory of the coalesced droplet, as shown in Figure 7a. Comparative evaluation demonstrated that the coalesced droplet's oscillation amplitude in the *y*-direction matched Droplet 1 but was 94.2% lower than Droplet 2 (Figure 7b). Additionally, the influence of the size difference between the two droplets on the suppression of oscillations in the *y*-direction was investigated (Figure S6). It is found that even with a two-fold volume difference, the suppression rate remains as high as 72.9%. These results confirm that droplet coalescence strategy can effectively suppresses longitudinal oscillations.

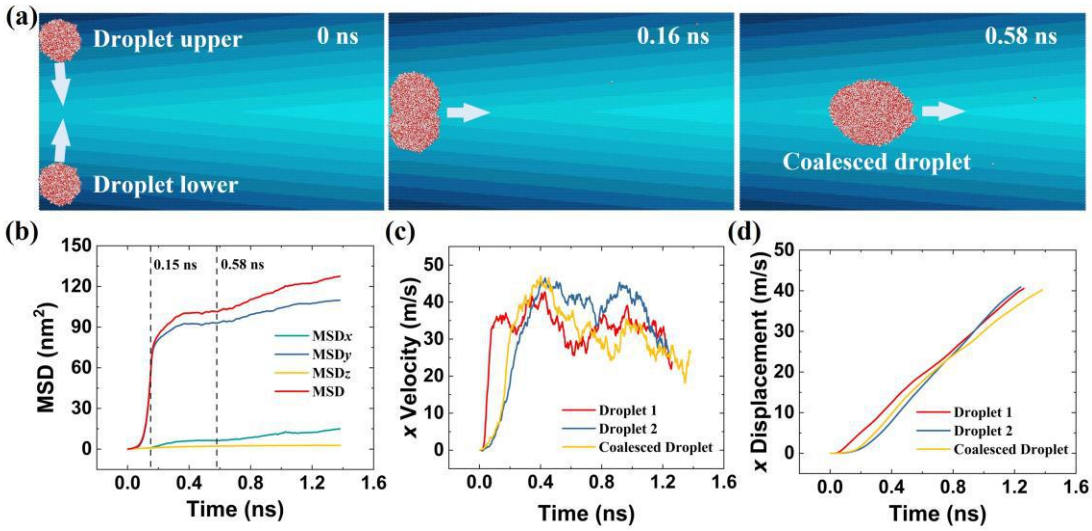



Figure 6 The coalescence process and self-transport behavior of two droplets on the DWPS. (a) The model of coalescence and self-transport of two droplets, both droplets have a volume equal to half that of an 8 nm diameter droplet, the initial coordinates (*x*, *y*) of droplets are (0, -11) and (0, 11) nm. (b) Mean squared displacement (MSD) of the two droplets versus time. (c) Time evolution of *x*-direction velocity and (d) displacement for Droplet 1, Droplet 2 and the Coalesced Droplet.

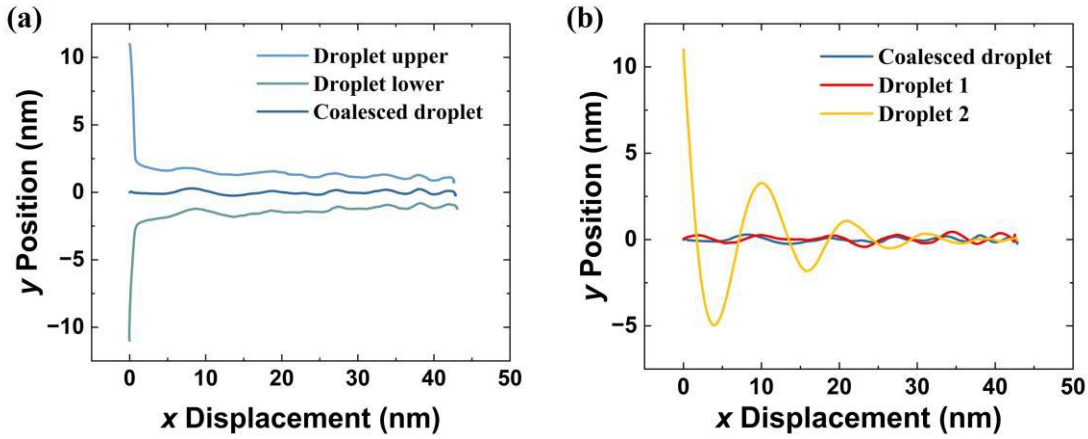



Figure 7 Active damping of *y*-oscillations by droplet coalescence strategy. (a) Temporal evolution of *y*-direction centroid positions of Droplet upper, Droplet lower, and the Coalesced droplet, the *y*-position curve of the Coalesced droplet represents the mean of the two original droplets' *y*-coordinates. (b) Temporal evolution of *y*-direction centroid positions for: Droplet 1, Droplet 2, and the Coalesced droplet.

**Performance Evaluation and Advantages of DWPS**

The DWPS essentially constitutes a surface with combined wettability and structural gradients. To investigate the differences in droplet self-transport performance between the dual-gradient surface and single wettability or single structural gradient surfaces, a wettability gradient surface (WGS) and a structural gradient surface (SGS) were further constructed, as shown in Figure 8. By observing the droplet transport behavior in Figure 2a, it was found that Droplet 1 only contacts wettability zones 1-5 (the wettability zones within the white wireframe in Figure 8a). Therefore, the WGS was divided into 20 equal parts from left to right, with wettability transitioning from zone 5 to zone 1 (Figure 8b). The SGS retained the outer wettability zones 4 and 5, while the original wettability zones 1-3 were all set to the wettability zone 1 (Figure 8c). Observing the droplet transport behavior on these three surfaces revealed that the SGS exhibited the fastest initial acceleration (Figure 9a). This is because, although termed a structure gradient, a significant wettability gradient still exists at the droplet's initial position, and this gradient is markedly steeper than on the other two surfaces. After the droplet moved beyond the initial steep wettability gradient at the tip, its velocity decreased rapidly. The time required to complete the 40 nm self-transport

exceeded twice that on the WGS, indicating the lowest transport efficiency (Figure 9b). In contrast, the droplet on the WGS accelerated quickly initially and then maintained a high velocity, reaching a maximum speed of 78 m/s, demonstrating the highest transport efficiency. However, compared to the other two surfaces, the droplet on the WGS was more susceptible to oscillations and molecular thermal fluctuations, causing deviation in the *y*-direction and making precise, targeted self-transport difficult to achieve (Figure 9c).




Figure 8 Three models for droplet self-transport: (a) DWPS with combined wettability and structural gradients, (b) wettability gradient surface (WGS), and (c) structure gradient surface (SGS). The white wireframe represents that the droplet only comes into contact with the wettability gradient surface within the wireframe during droplet transport.

The droplet self-transport behavior on these three surfaces was analyzed from the energy perspective. It was found that the solid-liquid interfacial interaction energy continuously decreased during transport on all surfaces, providing the driving energy (Figure 9d and Figure S7). Regarding the droplet's potential energy, it initially decreased at the start of motion on all three surfaces, contributing to the self-transport (Figure 9e). However, overall, the potential energy of the droplet on the DWPS remained largely unchanged. In contrast, the potential energy of the droplet on the SGS gradually increased with displacement. This indicates a competitive relationship between the solid-liquid interfacial interaction energy and the droplet's potential energy on the SGS, whereby a portion of the interfacial interaction energy is converted into potential energy rather than being fully utilized for droplet self-transport. This is one reason for the lower self-driving efficiency on the SGS. For the WGS, the droplet's potential energy gradually decreased, working in concert with the reduced interfacial energy to provide driving force, thereby enhancing the self-transport efficiency.

Examining the sum of the solid-liquid interfacial interaction energy and the droplet potential energy as a function of displacement (Figure 9f) shows rapid energy decrease during initial adsorption and acceleration at the initial position (pink region in Figure 9f). During the stable transport stage, the energy change approximated a linear relationship, allowing an estimation of the influence of the total energy change on the driving force. The energy decline rate $|dE/dx|$ for the WGS was approximately 2.15 times greater than that of the DWPS. Correspondingly, the average velocity during the high-speed transport stage (after 10 nm displacement) was about 2.3 times higher. For the SGS, the energy decline rate $|dE/dx|$ was comparable to the wettability gradient surface in the 10-30 nm displacement range, but this energy was primarily consumed by droplet deformation and surface adhesion. Upon entering the stable transport stage (after 30 nm displacement), the $|dE/dx|$ value was only 0.28 eV/nm. The $|dE/dx|$ for the WGS was about 9 times greater than that for the SGS, and its velocity during the stable stage was about 8 times higher. The energy decline rate $|dE/dx|$ is proportional to the transport velocity because the interfacial friction force $F_f$ is proportional to the velocity *v*. The energy decline rate provides the driving force for the droplet to balance the interfacial friction, thereby enabling approximately uniform motion of the droplet. Therefore, when energy reduction is harnessed for droplet self-transport, energy decline rate determines the droplet's acceleration and ultimate transport velocity.

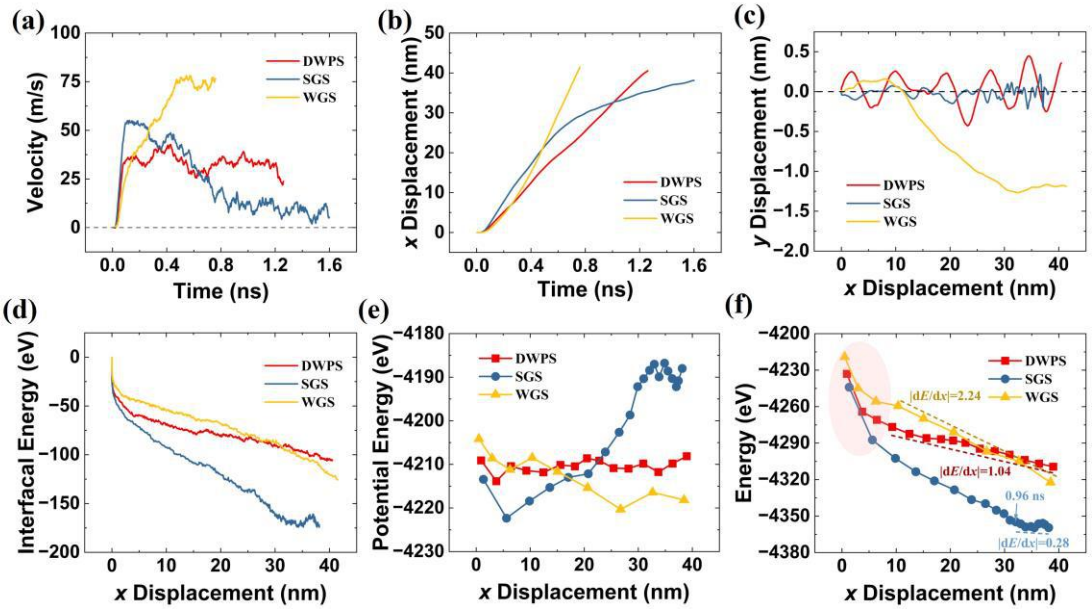



Figure 9 Comparison of droplet self-transport on the DWPS, SGS, and WGS. (a) Velocity and (b) displacement along *x*-direction versus time. (c) The *y*-direction displacement as a function of *x*-direction displacement of droplets for three surfaces. (d) Interfacial interaction energy between droplet and substrate surface, (e) droplet potential energy, and (f) their combined total energy as functions of droplet displacement.

The matching relationship between the droplet size and the characteristic dimensions of the textured substrate makes it challenging to transport small droplets efficiently over long distances. The influence of droplet size on the self-transport behavior on the DWPS was analyzed, as shown in Figure S8. Since the wettability of the DWPS is zone-specific rather than continuously varying, the transport velocity of larger droplets (6–8 nm) is more stable. The 5 nm droplet exhibits the fastest self-transport velocity and the highest efficiency. Although the 4 nm droplet shows the most significant velocity fluctuations, it can still achieve long-distance self-transport. A comparative study was conducted on the self-transport behavior of 4 nm small droplets on the DWPS with combined wettability and structural gradients versus SGS with only a structural gradient. The velocity and displacement of the droplets are shown in Figure 10. It can be observed that both surfaces exhibit considerable velocity fluctuations for small droplets. However, on the DWPS, the droplet undergoes multiple accelerations due to the wettability gradient and is transported to the far-right end of the surface,

achieving a displacement of 44.7 nm within 1.72 ns. In contrast, on the SGS with single structural gradient, limited by the matching relationship between the droplet and the structural characteristic dimensions, the maximum displacement is only 18.8 nm. Furthermore, the influence of the DWPS included angle $\alpha$ (ranging from 5° to 30°) on the long-distance self-transport of 4-nm-diameter droplets was investigated (Figure S9). The results show that increasing the angle $\alpha$ enhances both the transport velocity and stability, while successful long-distance transport is achieved across the entire range of angles. These results demonstrate that the DWPS with combined wettability and structural gradients can mitigate the influence of the matching relationship between the droplet and the textured substrate characteristics on the self-transport of small droplets, thereby facilitating long-distance self-transport of small droplets.

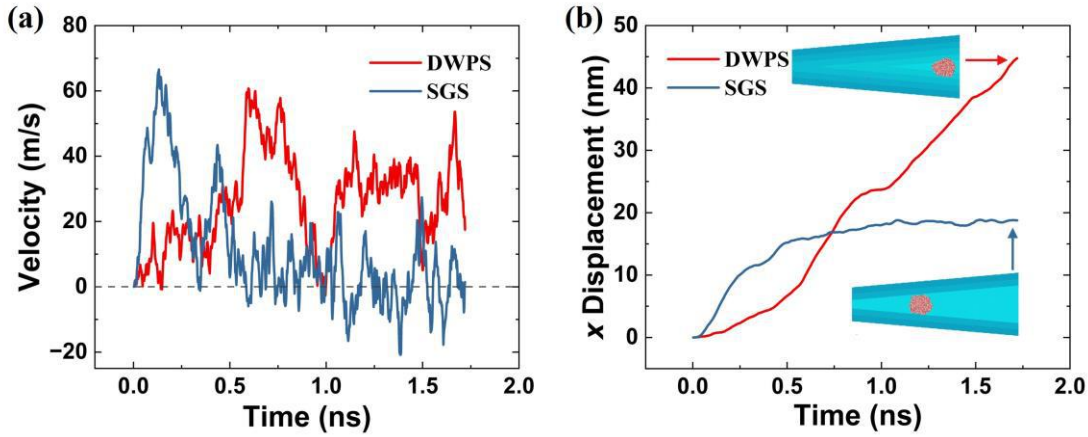



Figure 10 Promotion effect of DWPS with combined wettability and structural gradients on small droplet self-transport. (a) Droplet velocity and (b) displacement profile comparisons between DWPS and SGS for 4-nm-diameter droplets.

## Conclusion

In summary, we developed a DWPS incorporating both wettability and structural gradients, where the wettability gradient enables ultrafast droplet transport while the structural gradient rectifies the droplet transport direction, collectively achieving droplet rectification and ultrafast targeted self-transport. The periodic oscillations during droplet self-transport facilitate reversible conversion between kinetic energy and both droplet potential energy and solid-liquid interfacial interaction energy, thereby

enhancing transport efficiency. Theoretically, a relationship between interfacial friction force and droplet velocity, contact area, and solid-liquid interfacial interaction strength is established, providing deeper insights into the influence of interfacial friction on self-transport behavior. It is demonstrated that droplet coalescence effectively suppresses oscillatory motion and reduces periodic fluctuations during droplet self-transport. Compared to single wettability or structural gradients, the structural gradient surface exhibits the lowest transport efficiency, whereas the wettability gradient surface achieves the highest transport efficiency but is prone to deviation from the intended trajectory due to environmental disturbances. The DWPS combines the advantages of both, offering high transport velocity and precision. The mechanisms underlying self-transport behavior and efficiency variations across the three model surfaces are elucidated by analyzing the transition between synergistic and competitive relationships of solid-liquid interfacial interaction energy and droplet potential energy. Furthermore, the DWPS demonstrates superior capability in transporting small droplets compared to the single structural gradient surface. These findings provide a theoretical foundation for the design of functional surfaces aimed at achieving rapid and precise droplet self-transport.

## Declaration of Competing Interest

The authors declare that they have no known competing financial interests or personal relationships that could have appeared to influence the work reported in this paper.

## Acknowledgements

This work was supported by the National Natural Science Foundation of China (12272151, 52475301), Major Program of National Natural Science Foundation of China (NSFC) for Basic Theory and Key Technology of Tri-Co Robots (92248301), The Natural Science Foundation of the Jiangsu Higher Education Institutions of China (24KJB460010).

## Supporting Information

Supplementary data to this article can be found online.

Additional simulation details (Figure S1-S2); droplet transport velocity versus displacement (Figure S3); force and energy during Droplet 1 self-transport (Figure S4); energy during the coalescence and self-transport of two droplets (Figure S5); influence of droplet size on oscillation suppression (Figure S6); energy of droplet self-transport on DWPS, SGS and WGS (Figure S7); influence of droplet size on the self-transport behavior (Figure S8); influence of included angle $\alpha$ on droplet self-transport (Figure S9). (PDF)

Droplet rectification and targeted transport on DWPS (Movie S1). (MP4)

Oscillation suppression via droplet coalescence (Movie S2). (MP4)

## Data availability

Data will be made available on request.

## References


[1] Zheng, Y.; Bai, H.; Huang, Z.; Tian, X.; Nie, F.-Q.; Zhao, Y.; Zhai, J.; Jiang, L. Directional water collection on wetted spider silk. *Nature* **2010**, *463*, 640-643.

[2] Hou, L.; Liu, X.; Ge, X.; Hu, R.; Cui, Z.; Wang, N.; Zhao, Y. Designing of anisotropic gradient surfaces for directional liquid transport: Fundamentals, construction, and applications. *The Innovation* **2023**, *4*, 100508.

[3] Liu, C.; Sun, Y.; Huanng, J.; Guo, Z.; Liu, W. External-field-induced directional droplet transport: A review. *Adv. Colloid Interface Sci.* **2021**, *295*, 102502.

[4] Li, H.; Travlos, I.; Qi, L.; Kanatas, P.; Wang, P. Optimization of herbicide use: study on spreading and evaporation characteristics of glyphosate-organic silicone mixture droplets on weed leaves. *Agronomy* **2019**, *9*, 547.

[5] Yamada, Y.; Ishikawa, T.; Isobe, K.; Horibe, A. Droplet Transportation on Janus Harp Wires for Enhanced Fog Harvesting. *Small* **2025**, e06765.

[6] Mao, K.H.; Tao, Y.; Guo, W.S.; Yang, Q.S.; Zhao, M.Y.; Meng, X.Y.; Zhang, Y.H.; Ren, Y.K. Automatic detection of fluorescent droplets for droplet digital PCR: a device capable of processing multiple microscope images. *Analyst* **2024**, *149*, 5213-5224.

[7] Chen, H.; Zhang, P.; Zhang, L.; Liu, H.; Jiang, Y.; Zhang, D.; Han, Z.; Jiang, L. Continuous directional water transport on the peristome surface of Nepenthes alata. *Nature* **2016**, *532*, 85-89.

[8] Li, J.; Zheng, H.; Yang, Z.; Wang, Z. Breakdown in the directional transport of droplets on the peristome of pitcher plants. *Commun. Phys.* **2018**, *1*, 35.

[9] Chen, H.; Ran, T.; Gan, Y.; Zhou, J.; Zhang, Y.; Zhang, L.; Zhang, D.; Jiang, L. Ultrafast water harvesting and transport in hierarchical microchannels. *Nat. Mater.* **2018**, *17*, 935-942.

[10] Zhang, Q.; Bai, X.; Li, Y.; Zhang, X.; Tian, D.; Jiang, L. Ultrastable super-hydrophobic surface with an ordered scaly structure for decompression and guiding liquid manipulation. *ACS Nano* **2022**, *16*, 16843-16852.
[11] Hu, B.; Duan, Z.; Xu, B.; Zhang, K.; Tang, Z.; Lu, C.; He, M.; Jiang, L.; Liu, H. Ultrafast self-propelled directional liquid transport on the pyramid-structured fibers with concave curved surfaces. *J. Am. Chem. Soc.* **2020**, *142*, 6111-6116.
[12] Feng, S.; Zhu, P.; Zheng, H.; Zhan, H.; Chen, C.; Li, J.; Wang, L.; Yao, X.; Liu, Y.; Wang, Z. Three-dimensional capillary ratchet-induced liquid directional steering. *Science* **2021**, *373*, 1344-1348.
[13] Sun, Q.; Wang, D.; Li, Y.; Zhang, J.; Ye, S.; Cui, J.; Chen, L.; Wang, Z.; Butt, H.-J.; Vollmer, D.; Deng, X. Surface charge printing for programmed droplet transport. *Nat. Mater.* **2019**, *18*, 936-941.
[14] Zhu, H.; Zhang, J.; Cheng, Y.; Li, Q.; Xu, X.; Tang, B.; Liu, F.; Zhou, G. Lattice Boltzmann modeling of droplet actuation via temperature gradient and electrowetting. *J. Appl. Phys.* **2025**, *137*, 024701
[15] Huo, X.; Wang, Z.; Wang, Q.; Gu, J.; Wang, Q. Directional transport of water droplet on a programmed electrowetting-on-dielectric device. *Phys. Fluids* **2025**, *37*, 042112
[16] Wang, R.; Jin, F.; Li, Y.; Gong, J.; Lai, H.; Liu, Y.; Cheng, Z. Magnetic responsive on-site switching of the directional droplet self-transport in shape memory slippery tube. *Adv. Funct. Mater.* **2023**, *33*, 2305766.
[17] Wu, S.; Liu, J.; Wang, J.; Hao, D.; Wang, R. The Motion of Strawberry Leaves in an Air-Assisted Spray Field and its Influence on Droplet Deposition. *Trans. ASABE* **2021**, *64*, 83-93.
[18] Liu, X.; Jia, L.; Ding, Y.; Dang, C.; Yin, L.; Xu, J.; Zhang, R. Directional transportation behavior of droplets on a magnetically responsive micropillar array surface. *ACS Appl. Mater. Interfaces* **2024**, *16*, 56293-56303.
[19] Wu, J.; Li, X.; Lin, T.; Zhuang, L.; Tang, B.; Liu, F.; Zhou, G. Electric-field-induced selective directed transport of diverse droplets. *ACS Appl. Mater. Interfaces* **2024**, *16*, 4126-4137.
[20] Song, C.; Tao, X.; Chen, Y.; Mao, K.; Tao, Y.; Ge, Z.; Wen, H.; Chen, G.; Li, B.; Xue, R.; Jiang, X.; Zheng, X.; Ren, Y. Electrocapillarity-Induced Hurricane-in-a-Tube Enables the Generation and Patterning of Liquid Metal Droplets. *Adv. Funct. Mater.* **2024**, *34*, 2409341.
[21] Chen, K.; Jia, H.; Tian, Q.; Yang, F.; Ren, H.; Zhang, S.; Li, C. Asymmetric dynamic response of droplet impact on wedge microgrooved substrates. *Phys. Fluids* **2025**, *37*, 082006.
[22] Chen, K.; Jia, H.; Yang, F.; Ren, H.; Wu, F.; Li, C. Exploring mechanisms of asymmetric droplet impact dynamics on roughness gradient surface. *Phys. Fluids* **2024**, *36*, 112012.
[23] Omer, A.S.; Raza, A.; Zhang, T. Self-propelling water droplets on conical spikes with sawtooth surface structure. *ACS Appl. Mater. Interfaces* **2025**, *17*, 31604-31613.
[24] Hao, S.; Xie, Z.; Li, Z.; Kou, J.; Wu, F. Initial-position-driven opposite directional transport of a water droplet on a wedge-shaped groove. *Nanoscale* **2021**, *13*, 15963-15972.
[25] Zhang, X.; Ben, S.; Zhao, Z.; Ning, Y.; Li, Q.; Long, Z.; Yu, C.; Liu, K.; Jiang, L. Lossless and directional transport of droplets on multi-bioinspired superwetting V-shape rails. *Adv. Funct. Mater.* **2023**, *33*, 2212217.
[26] Cha, H.; Kim, M.-K.; Chang, H.C.; Zhang, L.; Miljkovic, N. Pinning-induced microdroplet self-transport. *ACS Nano* **2025**, *19*, 11049-11057.
[27] Zhang, F.; Liu, Z.; Gao, X.; Xu, J.; Zhang, Z.; Cheng, G.; Ding, J. Ultrafast self-propelled water droplet transport on a graphene-covered nanocone. *J. Phys. D: Appl. Phys.* **2021**, *54*, 505307.
[28] Ma, J.; Liu, K.; Dong, X.; Chen, C.; Qiu, B.; Zhang, S. Effects of leaf surface roughness and contact angle on in vivo measurement of droplet retention. *Agronomy* **2022**, *12*, 2228.

[29] Zhang, Z.; Zhang, F.; Huang, Q.; Cheng, G.; Ding, J. Ultrafast spontaneous driving of water droplets on monolayer graphene-covered gradient nanopillared surfaces. *Appl. Surf. Sci.* **2020**, *515*, 145976.
[30] Zhang, F.; Wang, Z.; Liu, Z.; Gao, X.; Song, Y.; Cheng, G.; Zhang, Z.; Ding, J. Cross-hatch textured cone enables Dual-Mode water transport and collection. *Chem. Eng. J.* **2023**, *478*, 147336.
[31] Li, J.; Li, J.; Sun, J.; Feng, S.; Wang, Z. Biological and engineered topological droplet rectifiers. *Adv. Mater.* **2019**, *31*, 1806501.
[32] Li, J.; Zhou, X.; Li, J.; Che, L.; Yao, J.; McHale, G.; Chaudhury, M.K.; Wang, Z. Topological liquid diode. *Sci. Adv.* **2017**, *3*, eaao3530.
[33] Hao, S.; Zhao, Z.; Xie, Z.; Li, Z.; Liu, J.; Wu, F.; Kou, J. Continuous and spontaneous directional droplet transport on bioinspired serial-wedge-shaped groove with wettability gradient. *Appl. Phys. Lett.* **2025**, *126*, 021601.
[34] Zhang, Y.; Nguyen, N.-T. Magnetic digital microfluidics – a review. *Lab Chip* **2017**, *17*, 994-1008.
[35] Li, Y.; Huang, J.; Cheng, J.; Xu, S.; Pi, P.; Wen, X. Enhanced movement of two-component droplets on a wedge-shaped Ag/Cu surface by a wettability gradient. *ACS Appl. Mater. Interfaces* **2021**, *13*, 15857-15865.
[36] Liu, L.; Xie, Z.; Wen, L.; Pi, P.; Qian, Y.; Wang, S.; Wen, X. Efficient collection and directional transport of condensate on superhydrophilic-hydrophobic surfaces with bioinspired hierarchical wedge-shaped channels. *Surf. Interfaces* **2024**, *55*, 105473.
[37] Zhang, Z.; Guo, X.; Tang, H.; Ding, J.; Zheng, Y.-G.; Li, S. Unidirectional self-driving Liquid droplet transport on a monolayer graphene-covered textured substrate. *ACS Appl. Mater. Interfaces* **2019**, *11*, 28562-28570.
[38] Papadopoulou, E.; Megaridis, C.M.; Walther, J.H.; Koumoutsakos, P. Ultrafast propulsion of water nanodroplets on patterned graphene. *ACS Nano* **2019**, *13*, 5465-5472.
[39] Sun, L.; Jing, D.-W. Directional self-motion of nanodroplets driven by controlled surface wetting gradients. *Phys. Fluids* **2023**, *35*, 052009.
[40] Mo, J.; Huang, H.; Wang, C.; Liang, J.; Li, Z.; Liu, X. Uphill directional passive transport of water droplets on axisymmetric surfaces. *Phys. Fluids* **2024**, *36*, 112021
[41] Horn, H.W.; Swope, W.C.; Pitera, J.W.; Madura, J.D.; Dick, T.J.; Hura, G.L.; Head-Gordon, T. Development of an improved four-site water model for biomolecular simulations: TIP4P-Ew. *J. Chem. Phys.* **2004**, *120*, 9665-9678.
[42] Hummer, G.; Rasaiah, J.C.; Noworyta, J.P. Water conduction through the hydrophobic channel of a carbon nanotube. *Nature* **2001**, *414*, 188-190.
[43] Subramanian, R.S.; Moumen, N.; McLaughlin, J.B. Motion of a drop on a solid surface due to a wettability gradient. *Langmuir* **2005**, *21*, 11844-11849.



https://dspace.org/

# Dual-gradient wettability-patterned surface for droplet rectification and targeted transport

**Zhang, Fujian; Cui, Baochen; Liu, Zhen; Huang, Kehan; Song, Yunyun ...**

**2025-11-25**
American Chemical Society (ACS)
https://doi.org/10.1021/acs.langmuir.5c04844
Zhang F, Cui B, Liu Z, et al., (2025) Dual-gradient wettability-patterned surface for droplet rectification and targeted transport. Langmuir, Volume 41, Issue 46, November 2025, pp. 31639-31648

Downloaded from a DSpace repository. https://dspace.org/